Mechanical and thermal design of the target neutral beam absorber for the High-Luminosity LHC upgrade

P. Santos Díaz,[1,*] F. Sanchez Galan,[2] R. De Maria,[2] E. Kepes,[3] P. Steinberg,[4] R. Longo,[5] S. Mazzoni,[2] F. Cerutti,[2] M. Sabate Gilarte,[6] A. Infantino,[2] B. Salvant,[2] M. Murray,[7] O. Boettcher,[2] J. Hansen,[2] V. Baglin,[2] N. Zelko,[2] E. Bravin,[2] H. Mainaud,[2] P. Bestmann,[2] A. Herty,[2] P. Fessia,[2] and M. Gonzalez de la Aleja Cabana[2]

[1]*National University of Science and Technology "MISIS", 119049 Moscow, Russia*
[2]*CERN, 1211 Geneva, Switzerland*
[3]*CEITEC—Central European Institute of Technology, 61600 Brno, Czech Republic*
[4]*Brookhaven National Laboratory, 11973 Upton, New York, USA*
[5]*University of Illinois at Urbana Champaign, Champaign, 61820 Illinois, USA*
[6]*University of Seville, 41004 Seville, Spain*
[7]*University of Kansas, Lawrence, 66045 Kansas, USA*

(Received 8 April 2022; accepted 25 April 2022; published 13 May 2022)

The High-Luminosity target neutral beam absorber (TAXN) is the radiation absorber of the neutral particle debris generated at the beam collisions carried out in the ATLAS and CMS detectors at the Large Hadron Collider (LHC). The new absorber will protect the superconducting magnets from this radiation to prevent their quenching at a design luminosity of 7.5×10^{34} cm^{-2} s^{-1}. This article describes the mechanical design of the TAXN assembly and the recombination chamber together with the thermal computations performed for the water-cooling and bakeout system prepared for the engineering design review held in January, 2021. It takes into account the internal integration of the zero degree calorimeter and beam rate of neutrals luminosity detector as well as their physics case overview. In addition, it provides the beam aperture breakdown and the heat deposition expected in the absorber.

DOI: 10.1103/PhysRevAccelBeams.25.053001

I. INTRODUCTION

The Large Hadron Collider (LHC) at CERN produces proton-proton collisions with a 13 TeV center-of-mass energy. The High-Luminosity LHC project aims to increase the instantaneous luminosity of the LHC's nominal value by a factor of 5 while also increasing the energy (up to the design value of 14 TeV center of mass) and the integrated luminosity per year [1]. The upgrade will mainly be focused around the long straight sections (LSSs) of the LHC on both sides of ATLAS and CMS [two of the four interaction points (IPs) located along the 27 km particle accelerator]. A crucial step of the upgrade will be the replacement of the current LHC neutral beam absorber (TAN) by an updated design adapted to the High-Luminosity conditions (TAXN) [2]. In fact, four new TAXNs (one per each side of both IP1 and IP5) will be installed inside the LSSs during the long shutdown 3.

The TAXNs, shown in Fig. 1, are 30 t absorbers composed of nine subassemblies. Each subassembly weights less than 5 t. The position of each subassembly is adjusted using customized pins. The stainless-steel recombination vacuum chamber [3] is located at the center of the inner assembly of a TAXN (i.e., the absorber box), and it is clamped inside two water-cooled absorber copper clamp shells. The recombination chamber is 4.3 m long and possesses a large aperture facing the interaction point which smoothly transitions into two tubes on the side facing away from the IP. Both the copper absorber and the whole stainless-steel recombination chamber are surrounded by heating jackets for bakeout purposes. An assembly composed of five carbon-steel (St-36) shielding blocks surround the absorber box for radiation protection: two base plates (lower and upper), two lateral shields, and the top cover. Two marble blocks are located on the two ends of the IP which provide a personnel lower-radiation area inside the long straight section. Finally, the complete assembly is supported by three jacks, which can be remotely aligned to optimize the recombination chamber's beam aperture. The four TAXNs are identical except for the survey brackets' side position of the top cover and the jacks' height, which are customized to adapt the design to the wire positioning system's location and the beam line

*pablo.santos.diaz@cern.ch

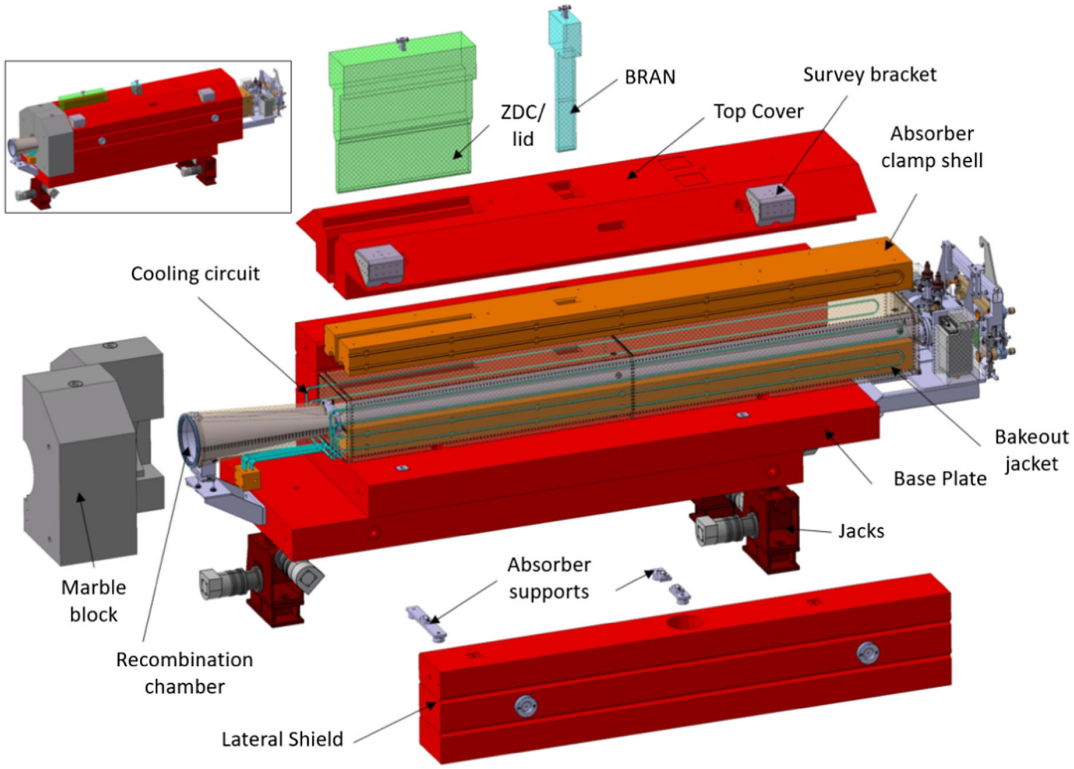

FIG. 1. TAXN overview. The detector geometries represent a space reservation only.

height (1100 mm in ATLAS and 950 mm in CMS LSSs, respectively).

There are two open slots inside the TAXN which are accessible from the top. The open slots will host the luminosity and forward physics detectors. A new beam rate of neutrals (BRAN) relative luminosity monitor and a zero degree calorimeter (HL ZDC) are integrated within the new design. The BRAN is foreseen to remain installed during the complete LHC run. Meanwhile, the HL ZDC will be in place only during the Pb-Pb runs. During proton-proton runs, the HL ZDC slot is covered by a lid to provide radiation protection to the personnel and equipment.

II. MECHANICAL DESIGN, HEAT DEPOSITION, AND BEAM APERTURE BREAKDOWN

The mechanical design of the TAXN has been adapted to protect the downstream cryogenic magnets, to integrate the recombination chamber, and to reuse the current TAN shielding to avoid wasting about 85 t of radioactive carbon steel.

A. Constraints and requirements

The main constraints and functionalities which the design shall comply with are as follows. (i) The heat loads from IP collision debris. The energy deposition mainly originates from neutral particles impacting on the absorber block. This translates to a heat load of 1.4 kW distributed along the copper block as shown in Fig. 2. The total power deposited onto the whole TAXN is 1.8 kW. Consequently, in order to maintain the absorber temperature below 85°C following vacuum requirements, a cooling system (described in Sec. IV) is to be included in the mechanical design. The length of the absorber and the beam pipe separation of the recombination chamber protect the downstream magnets from collision debris. Meanwhile, the heat load received by the surrounding collimators can be extracted by their cooling system. An internal aperture of 88 mm diameter fulfills the machine protection requirements [4]. (ii) The integration of the bakeout system, described in Sec. III, is required to achieve the desired vacuum conditions for the LHC's operation. (iii) The transverse beam aperture and impedance limits for the LHC proton-proton and Pb-Pb beams (discussed in Sec. II C). The beam aperture of the HL LHC layout v1.5 flat optics at 14.0σ is shown in Fig. 3. The 12.5σ expected upstream in the inner triplet and dipole 1 shows that there is a margin of 1.5σ in terms of aperture. (iv) The expected highly radioactive environment. (v) The remote alignment system of the TAXN itself and its neighboring components. (vi) The integration and operation of the HL ZDC and BRAN detectors to provide an optimized environment for the full exploitation of their functionalities. (vii) The LHC operation and the tunnel integration as shown in Fig. 4.

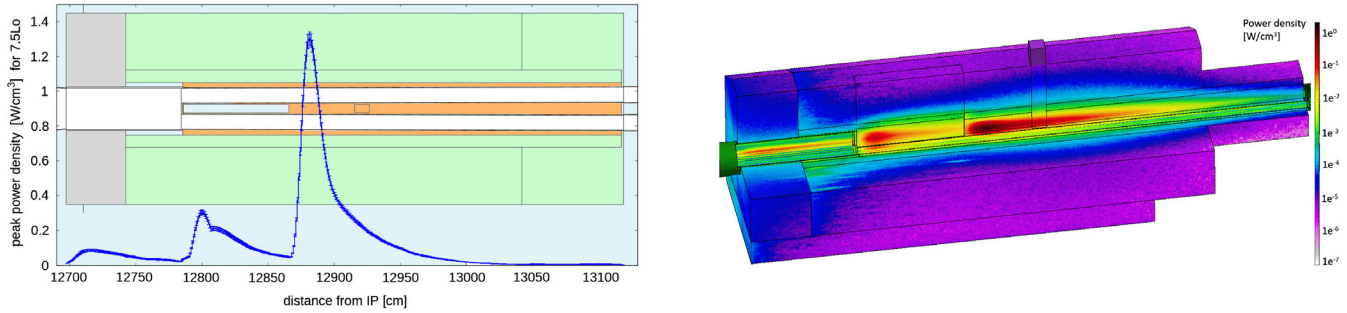

(a) (b)

FIG. 2. Heat load originating from the collision debris calculated using FLUKA [5,6]. (a) Heat deposition peak distribution along the beam machine axis. (b) Heat deposition distribution along the transverse plane of the particles beam.

B. TAXN design

The top cover, which has been adapted for the integration of the HL ZDC and BRAN detectors, is the only new shielding part to be fabricated. The remaining "U-shaped" iron shielding will be recycled from the existing LHC TAN. The shielding blocks are positioned by alignment keys and secured by tightening rods, while the absorber block rests on the shielding base plate on three supports (Fig. 5).

The three sphere-based absorber supports are coupled with a slot, round, and plane geometries, respectively, maintaining the support on the IP side as the fixed point [Fig. 5(a)]. This design allows the absorber's dilatation in the traversal and longitudinal directions during the bakeout cycle heating while ensuring that it returns to its initial position after the bakeout cycle's completion, i.e., when the absorber returns to room temperature. The absorber inserts

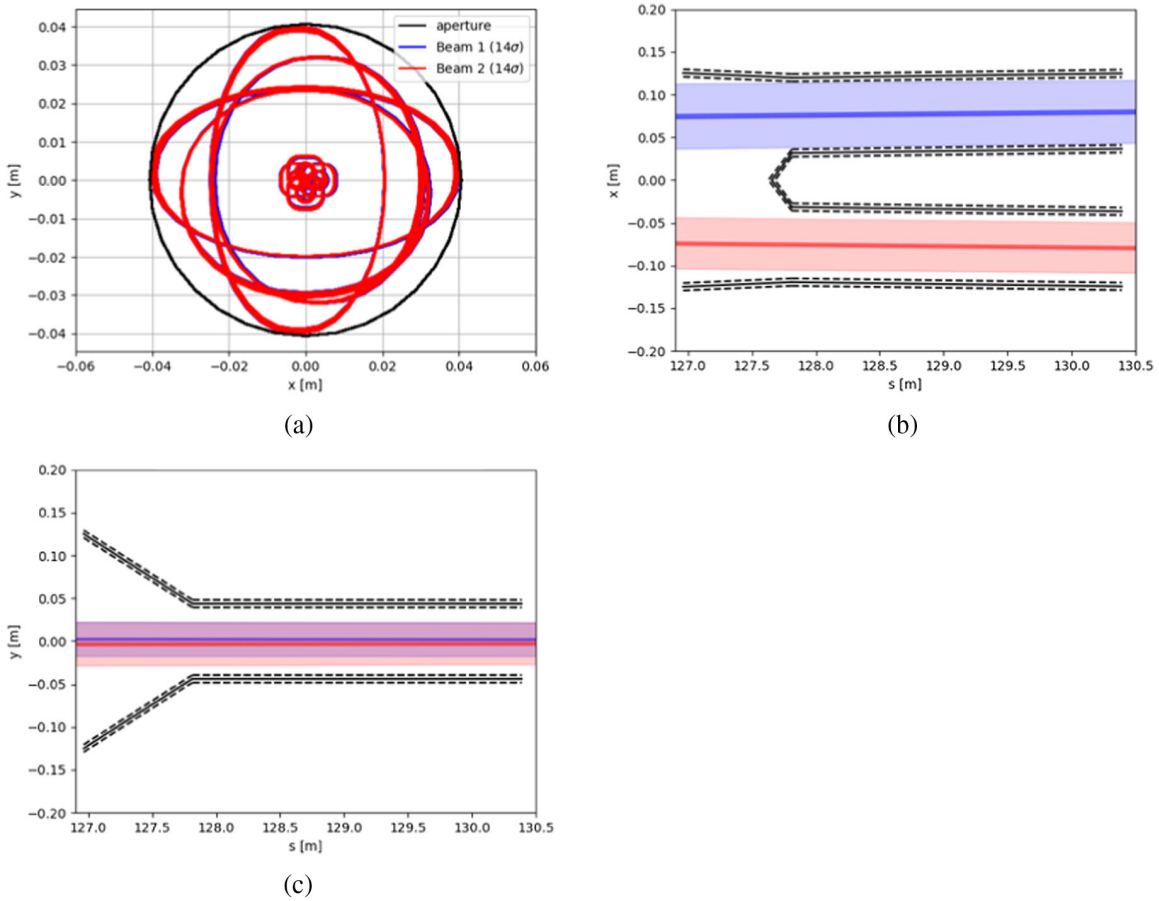

(a) (b)

(c)

FIG. 3. Beam size inside the 88 mm internal diameter double pipes of the recombination chamber for flat optics at 14.0σ. (a) Vertical transverse cross-section of the particles beam. (b) Longitudinal horizontal cross-section of the particles beam on the right side of CMS. (c) Longitudinal vertical cross-section of the particles beam on the right side of CMS.

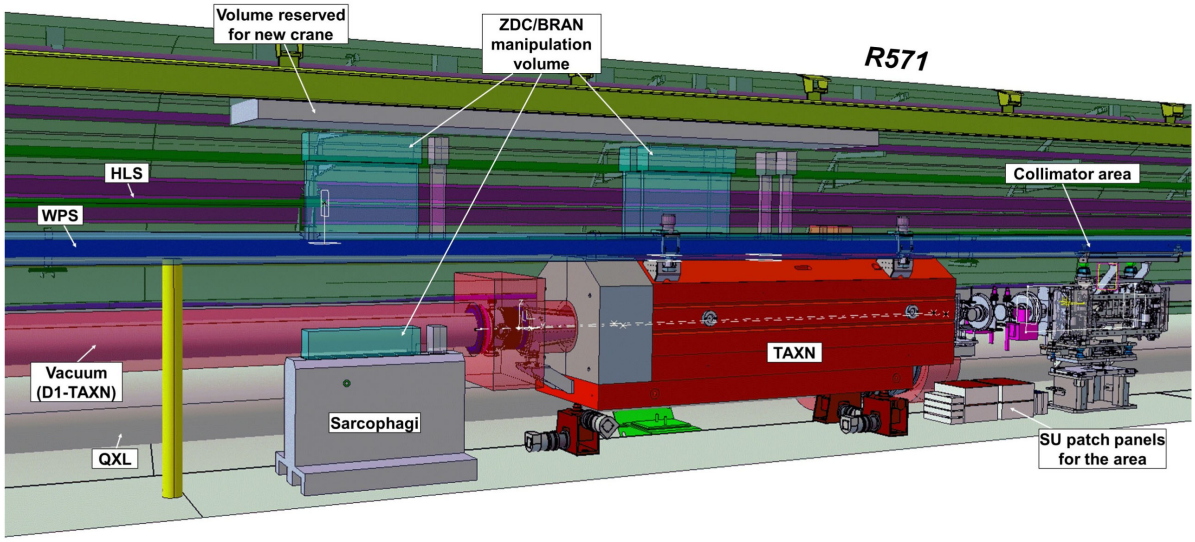

FIG. 4. TAXN integration inside the LHC tunnel.

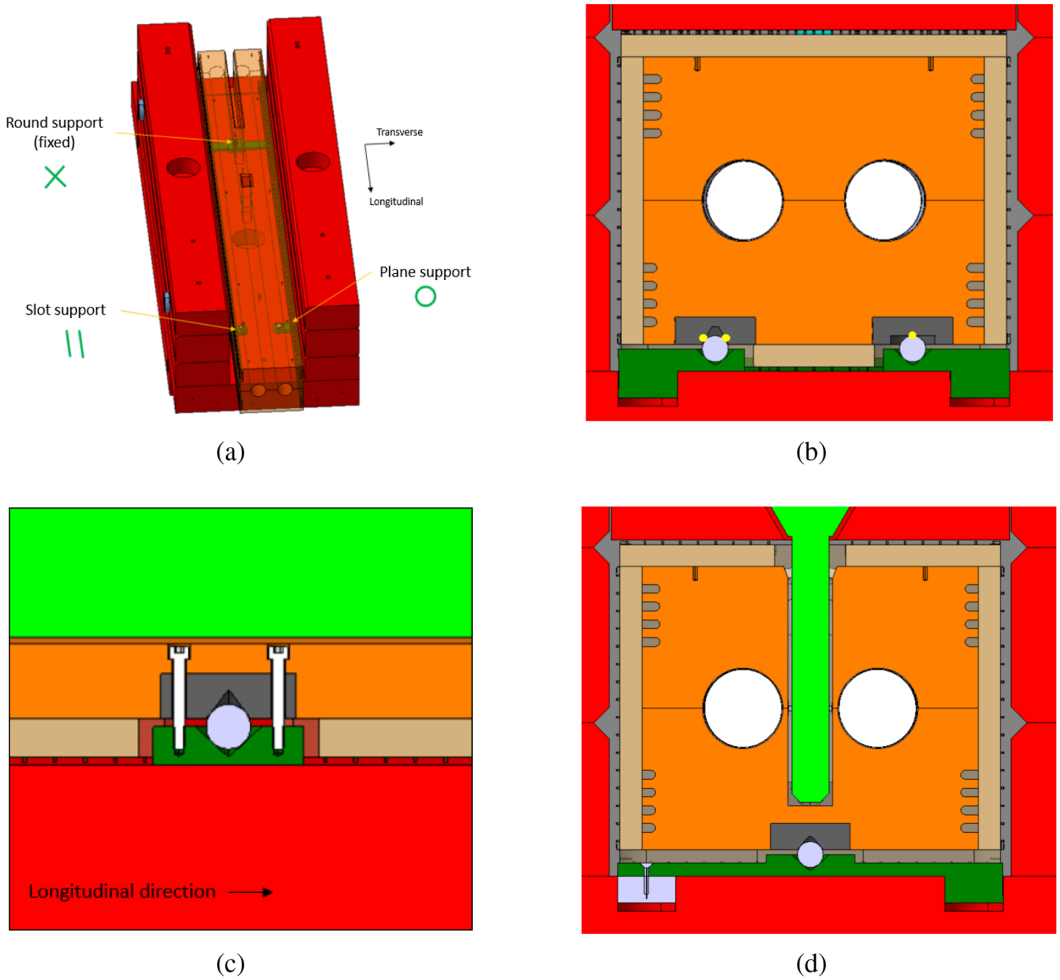

FIG. 5. Absorber support description. (a) General scheme of the absorber supports conguration. (b) Slot and plane supports (transverse cross section). (c) Round support (longitudinal cross section) (d) Round support (transverse cross section).

TABLE I. Summary of the main materials used in the construction of the TAXN.

Part	Material or alloy
Absorber	Electrolytic tough pitch copper
Cooling pipes	$CuNi_{10}Fe_1Mn$
Shielding	American Society for Testing and Materials A36 steel or ENS275
Vacuum chamber	Stainless steel 316LN and/or 304L Cu and NEG coated
Marble block	Marble
Bakeout jackets	Type E glass-fiber insulation plus nickel-chrome heating element
Absorber inserts	$EN34CrNiMo_6$ steel
Support spheres	American Iron and Steel Institute 420C stainless steel
Absorber supports	Alu EN AW-6082 (T6)
Survey brackets	Stainless steel

are foreseen to assure repeatability. In addition, since the inserts are made of soft copper (relative to the hard steel of the spheres), abrasion of the absorber during the bakeout cycles is also prevented. There is a two- and one-"point" contact between the slot and plane, respectively, as highlighted by the yellow dots in Fig. 5(b). Meanwhile, the round fixed sphere is in contact along its whole circumference. Consequently, high stresses will appear along the contact regions of the spheres in both the absorber and the support. This has been addressed by the well-established V-shaped couplings found in the LHC collimators. These couplings include hardened nitride steel inserts with a minimum average hardness of 60 HRC. In addition, an aluminum support with an extended contact surface houses the steel sphere on which the inserts will rest. The collimator's V-shaped couplings, which correspond to the present slot geometry, have two contact points which were tested for a 7 t vertical load [7]. Meanwhile, the absorber and the bakeout jackets' total weight is about 3.5 t. Nevertheless, a final test with a single contact point is recommended for the final validation of the concept.

Moreover, the absorber-recombination chamber assembly has to withstand a maximum of 500 kg of vacuum forces along the longitudinal direction induced by the cross section transition along the vacuum chamber when the corresponding vacuum sector is under vacuum up to the double pipe flanges. In consequence, two M8 screws (class 8.8) with a total shear plane resistance of 14.1 kN are fixed to the round absorber support [Fig. 5(c)]. Therefore, the absorber is rigidly fixed to the round support in the vertical direction as well.

The current TAN shielding, which is going to be partially reused, has four supporting points for the absorber. On the contrary, the new design includes only three support points while aiming for an isostatic concept. Therefore, the round support assembly converts the two hole supports into a single one through a two-piece assembly [highlighted in green and gray in Fig. 5(d)] that can be adjusted to the real holes' separation by a screw-slot coupling.

The highly radioactive environment demands an accurate selection of the materials used in the design of the TAXN assembly: First, the activation and, therefore, the individual effective dose during maintenance or interventions must be minimized; second, the amount of future radioactive waste should be kept as low as possible. CERN recommends to limit the cobalt content in stainless steels to a guideline value of ≤ 0.1 wt%, when possible, and prohibits cobalt contents above 0.3 wt%. Thus, the design of the device is optimized according to the as low as reasonably achievable (ALARA) principle. Table I lists the core materials of the main parts of the TAXN assembly. Radiation protection FLUKA simulations [8] have been performed to assess the residual dose rate expected during the access to the HL LHC tunnel and maintenance or operation of the TAXN. Residual ambient dose equivalent rates in contact with the TAXN can reach up to the mSv/h level.

The TAXN is aligned remotely. Hence, it must comply with the LHC sector alignment strategy. Consequently, vacuum modules equipped with bellows are installed in the beam line on both sides of the TAXN. Survey brackets for the vertical sensors and the wire positioning system's (WPS) support together with two inclinometers have been included in the top cover design. Three motorized jacks carry the complete assembly, making the TAXN a remotely aligned component. In addition, two fiducial supports on the side shielding are integrated for a smooth alignment connection between the alignment of the long straight section and the dispersion suppressor region. Besides, alignment references are distributed along the external surface of the shielding, absorber, and the recombination chamber for the fiducialization process.

An 800 mm slot and a 110 mm slot within the absorber and shielding are foreseen for the HL ZDC and BRAN, respectively. The interfaces among the detectors and the TAXN have been identified [9], and a space reservation for each detector has been defined, which take into account the detectors' handling procedure, radiation protection, and integration constraints inside the LHC tunnel (Fig. 4). The high expected radioactive doses in the TAXN's vicinity force the remote control of the detectors' replacement. A customized crane is to be developed for the handling of the detectors to allow an ALARA approach during the

TABLE II. Summary of the mechanical and alignment tolerances used to determine the beam aperture. All tolerances are given considering the diameter, with respect to the zero line between the beam lines and for A, B, and C locations described in Fig. 6.

		Accuracy or standard manufacturing tolerance [mm]	
Tolerance type	Concept	A	B and C
Alignment	Precision of the measurement from the measured reference axis to the fiducials at 3σ	0.1	0.1
	Precision of the transfer measurement from the fiducials to the permanent monitoring system at 3σ	0.15	0.15
	The alignment precision with respect to the neighboring element (via WPS and inclination sensors) at 3σ	0.9 (Q5-Q5)	0.9 (Q5-Q5)
Mechanical	Pipe thickness	0.2	0.2
	Pipe circularity [10]	1	1
	Position of the pipes with respect to each other		Not applicable
	Reference plate holes	0.5	
	Welding of the pipes to the reference plate	1.5	
	Absorber groove cylindricity [11]	Not applicable	1.8
	Bakeout cycle returning position (theoretical)	0.5	0.5
	Remaining movements of the absorber with respect to the shielding (theoretical)	0.5	0.5
	Maximum shimming adjustment offset	0.7	0.7
		6.05	5.85

detectors' exchange and maintenance. Bevels and chamfers have been included in the absorber and top cover slot's corners to facilitate the insertion of the detectors and to avoid any stacking. The lid and detectors will be stored in a radiation-protection shielded sarcophagus when they are removed from the TAXN to minimize personnel exposure.

C. Recombination chamber

The main function of the recombination chamber is to smoothly combine two pipes into a single one without inducing any instability on the beam under the HL LHC operational vacuum pressure. The recombination chamber's mechanical aperture should be minimized to allocate the absorber as close as possible to the beam and, consequently, to protect the downstream superconducting magnets. Meanwhile, the recombination chamber's mechanical aperture must be large enough to let the beam through the chamber avoiding any damage to the tube's surface. Hence, a compromise between the two constraints must be reached. In addition, the recombination chamber's geometry must respect the two beams' separation at two specific locations along the chamber's length, namely, at 151.1 and 161.1 mm of the absorber longitudinal extremities having nonparallel double pipes. Consequently, a precisely machined reference plate and a welded plate will define the mechanical separation between the two pipes at the beginning and the end of the absorber. The mechanical tolerances' definition of the absorber and the pipes (listed in Table II) are crucial for an efficient heat transfer during bakeout. The absorber and recombination chamber's tolerances are defined in such a way that, in the worst-case scenario, a maximum gap of 0.25 mm between the absorber and the chamber pipes is expected. If required, the gap will be filled during the assembly with a thin copper foil ensuring full contact between the copper and the pipe for an efficient heat transmission and optimized alignment of the vacuum chamber.

The design will ensure that the mechanical aperture of the beam pipe is larger than the beam, considering the mechanical and alignment tolerances [12]. The applied mechanical and alignment tolerances used inside the double pipes are detailed in Table II. The position of the pipes with respect to each other is controlled by the absorber grooves along the absorber's length (positions B and C). Meanwhile, at the reference plate's position (indicated in Fig. 6 by label A), the pipes' position will be given by the plate machining accuracy and the double pipes' welding assembly. The linear sum of the mechanical and alignment tolerances (at 3σ) equals 6.05 mm at the reference plate, which corresponds with the worst-case location in terms of the beam aperture. Thus, as the nominal diameter of the double pipes is 88 mm, the free mechanical aperture available to the beam cross section is about 82 mm, considering that the beam is centered to the mechanical pipe's axis.

The shape of the recombination chamber is also influenced by beam concerns regarding the coupling impedance. In fact, the interaction between the electromagnetic fields generated by the powerful HL LHC beam and the walls of the recombination chamber give rise to wakefields that can cause beam instabilities and/or beam-induced heating of the vacuum chamber itself. Such phenomena can limit the performance of the HL LHC and should, therefore, be minimized. The impedance of the recombination chambers installed for the first LHC runs was

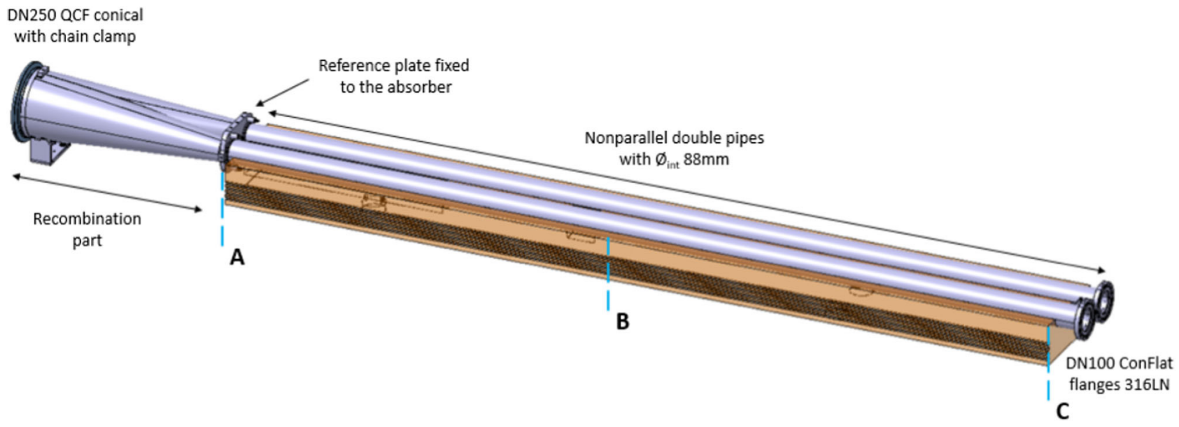

FIG. 6. Recombination chamber design inserted in an absorber clamp. A, B, and C indicate the tolerance breakdown described in Table II.

studied and optimized [13]: The ideal shape is the gradual, smooth merging of the two smaller pipes into the bigger one. In practice, this shape is described by the intersection of the two smooth tapers defined between each smaller pipe and the larger pipe, yielding a parabola-shaped wedge. The maximum allowed tapering angle is specified at 15 °C for LHC and HL LHC in order to reduce the large impedance contribution caused by abrupt transitions. Simulations of the new recombination chamber revealed significant convergence issues and difficulties hindering the comparison of the solutions owing to the large difference between the pipe radii at the two ends of the recombination chamber [14]. The solution was found by simulating two recombination chambers joined by a long, large pipe to recover the same input and output pipe dimensions for the simulation model. Thus, it could be shown that no significant resonant modes are linked to the recombination chamber's proposed geometry. In addition, the effective impedance contribution of two recombination chambers were of the order of 5 kΩ/m in the transverse plane and 0.06 mΩ in the longitudinal plane, which are deemed to be reasonable contributions for such accelerator components [15].

The chamber is made of SS316LN and/or SS304L steel alloys TIG welded, while the tube legs can be rolled and electron-beam welded owing to the mechanical tolerances and vacuum requirements. The complete inner surface of the chamber is flash gold-plated to enable the sticking of a minimum of 5-μm-thick copper layer. The copper layer is required for the beam current's continuity. Finally, the inner surface in contact with vacuum is non-evaporable getter (NEG) coated with a Ti-Zr-V film ($\approx 30, 30, 40\%$) to guarantee a homogeneous pumping speed under ultrahigh vacuum conditions.

The chamber is attached to the absorber by four bolts at the reference plate location which define only its longitudinal position with respect to the absorber. Between the reference plate and the absorber, there are four spacers used for the integration of the bakeout jacket. In addition, two supports for the recombination chamber and the downstream vacuum modules compatible with the bakeout dilatation and alignment requirements are included at the TAXN extremities.

III. BAKEOUT SYSTEM

The average gas density along the long straight sections I and V must ensure that the background to the LHC experiments remains at acceptable levels [16,17] considering the HL LHC beam parameters. Thus, the recombination chamber and all the room-temperature components under vacuum will be heated in order to activate the NEG coating and achieve the requested ultrahigh vacuum pressure. This process is referred to as the bakeout cycle [18]. Consequently, a bakeout system is to be integrated in the TAXN through which the chamber can reach 250 °C in 5 h.

A. Analytical calculations

Every source of the heat losses from the bakeout jackets to the tunnel have been considered to exhibit their worst-case scenario. However, heat losses through the chamber to its adjacent vacuum components have not been considered, as they should be at the same temperature (since they belong to the same vacuum sector). The applied model assumes that the lid and BRAN are inserted into their respective slots during the whole bakeout cycle. Figure 7 shows the scheme of the thermal resistances identified in this study. The black dots between the resistances correspond to the different temperatures along the thermal circuit.

The considered heat conduction losses comprise the bakeout jacket losses $Q_{L.j}$, since the jackets are not perfect insulators; the conductive absorber supports losses $Q_{L.\mathrm{as}}$ (the absorber is supported by three feet attached to the shielding); and the radioactive plus convective losses through the ZDC and BRAN slots $Q_{L.\mathrm{BRAN}}$ and $Q_{L.\mathrm{ZDC}}$, respectively. A perfect thermal contact between the components was assumed (although nonconservative, for the sake of simplicity). The convective and conductive, $Q_{L.i}$, and radiation, Q_{rad}, losses were computed according to

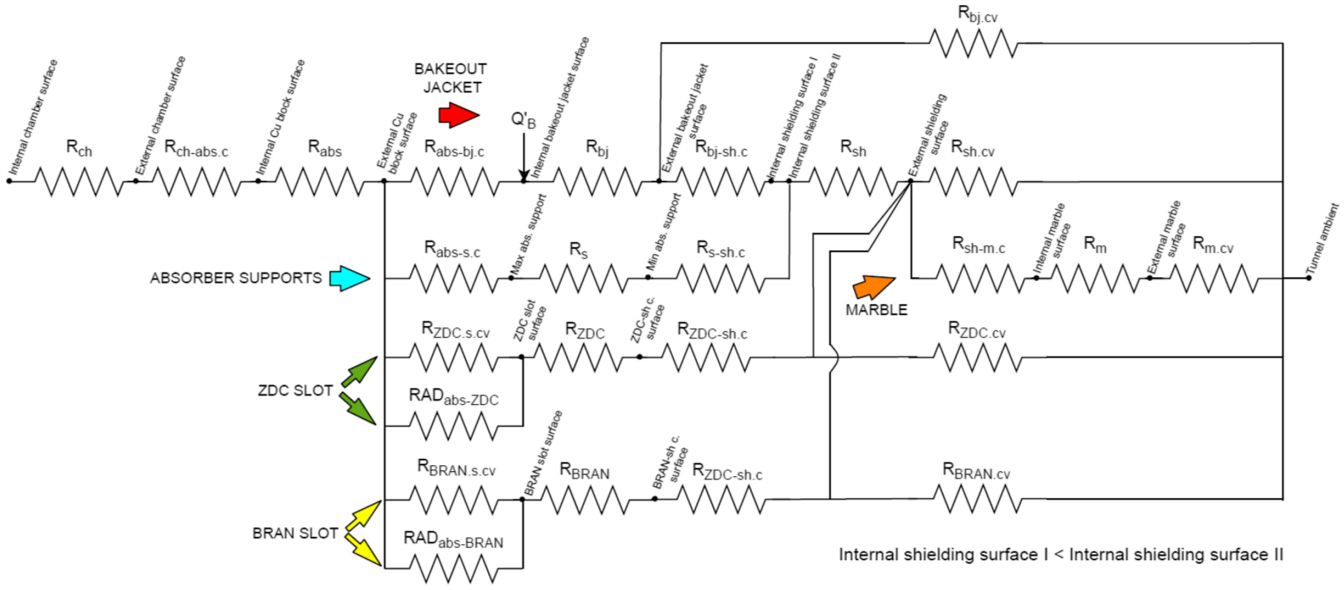

FIG. 7. Resistance diagram of the bakeout system.

Eqs. (1) and (2), respectively, where T_i refers to the temperatures during the bakeout cycle and R_i denotes the thermal resistances. Equation (2) is the basic net rate of heat transfer by radiation of a gray body. The intrinsic heat needed to warm up the copper block, $Q_{\mathrm{Cu.heating}}$, is expressed by Eq. (3), where $c_{p.\mathrm{Cu}}$ is the specific heat of copper, m_{Cu} is the absorber copper mass, and t_{bake} is the duration of the bakeout. Last, the total power required to heat up the copper block is given by the sum of the heat losses and the intrinsic heat necessary for warming it up [Eq. (4)]. The lost heat is transferred to the shielding, marble, and detectors and is released to the ambient air inside the tunnel via convection.

$$Q_{L.i} = \frac{T_1 - T_2}{R_i}, \tag{1}$$

$$Q_{\mathrm{rad}} = \sigma \varepsilon_{12} A_1 F_{1\to 2}(T_1^4 - T_2^4), \tag{2}$$

$$Q_{\mathrm{Cu.heating}} = \frac{c_{p.\mathrm{Cu}} m_{\mathrm{Cu}} (T_0 - T_{\mathrm{bake}})}{t_{\mathrm{bake}}}, \tag{3}$$

$$Q_{\mathrm{bake}} = Q_{\mathrm{Cu.heating}} + Q_{L.j} + Q_{L.\mathrm{as}} + Q_{L.\mathrm{BRAN}} + Q_{L.\mathrm{ZDC}}. \tag{4}$$

Figure 8(a) shows the power supply required along the bakeout cycle analytically computed using a PYTHON code [19] for a simplified bakeout cycle. The red curve indicates the simplified bakeout temperature which the system will achieve. The green, light blue, and yellow curves show the copper's intrinsic heat, radioactive losses, and convective or conductive losses, respectively. The sum of the three curves

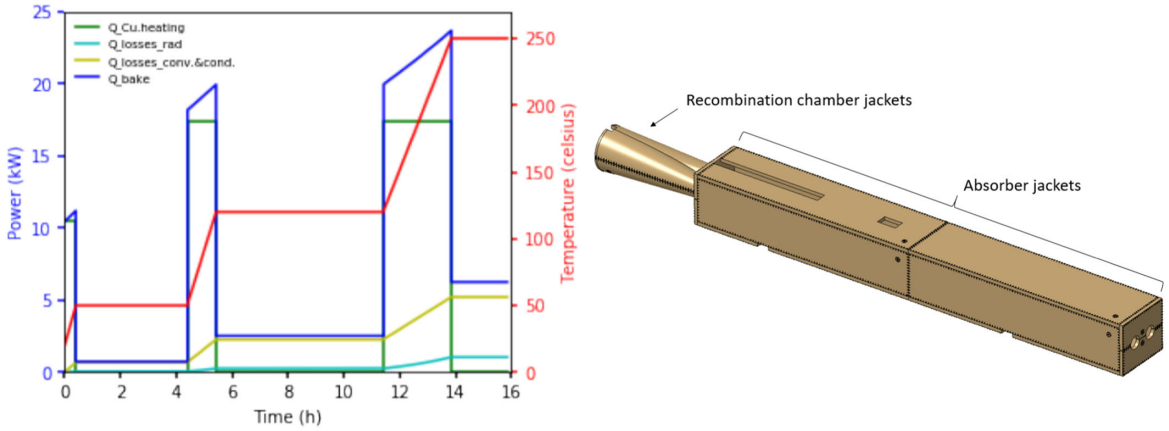

(a) (b)

FIG. 8. Bakeout. (a) Power supply during the bake-out cycle on the absorber jackets. (b) Bake-out jacket assembly.

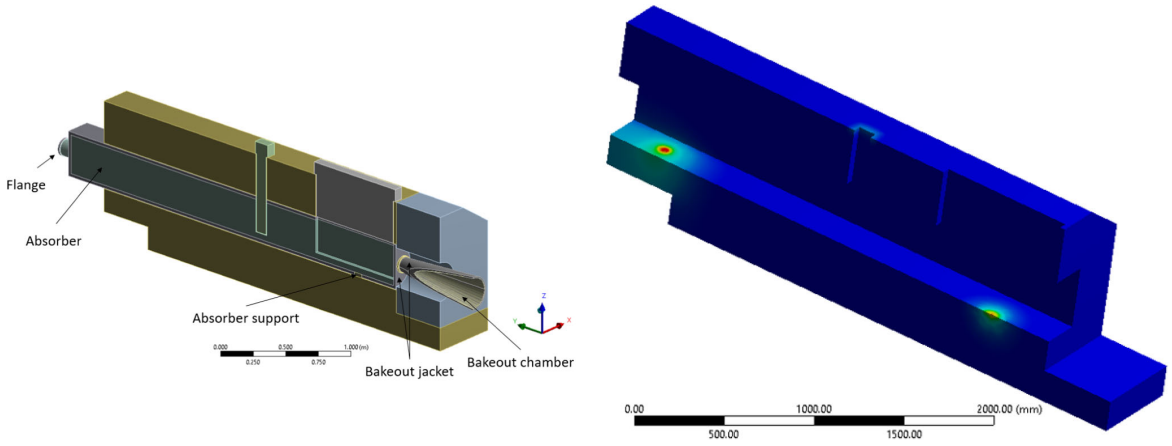

(a) (b)

FIG. 9. Bakeout simulation. (a) 3D simulation model for the bake-out cycle. (b) Temperature map of the shielding during the bake-out process.

indicates the total power to be provided by the heating jackets (dark blue curve). In conclusion, the maximum power (without including a safety margin) required during the bakeout cycle is 24.4 kW, where 23.7 kW, 600 W, and 100 W are consumed by the absorber jackets, recombination chamber jackets, and the flange collars, respectively.

The proposed bakeout system consists of 14 LHC bakeout jackets [20] to provide the required power and insulation [see Fig. 8(b)]. Furthermore, type E thermocouples [21] are to be incorporated along the chamber and absorber to monitor the temperature during the bakeout process.

B. Computational thermal analysis

A transient thermal analysis has been carried out in ANSYS WORKBENCH [22] to evaluate the performance of the proposed bakeout system.

The detailed 3D model shown in Fig. 1 has been simplified by slightly modifying its geometry and longitudinally cut so that only the symmetric half of the TAXN [Fig. 9(a)] is kept with the aim of reducing the computational resources required for solving the model. The material properties of each part (except for the bakeout jackets) have been taken from the ANSYS library. The BRAN detector was considered as a solid copper block for the sake of simplicity. Table III shows the material and mesh size of each component. Mainly, Hex20 elements were used for all bodies except for the vacuum chamber, which consisted of shell elements. The average mesh quality of the model given by the software was 83%.

TABLE III. Materials and mesh size used in the bakeout ANSYS model.

Component	Material	Mesh size [mm]
Absorber	Copper	10
Bakeout jacket	E-glass fiber [20]	10
Absorber support	Stainless steel	25
Marble block	Marble	50
Shielding	Iron	50
BRAN	Copper	10

The initial temperature of the model was assumed to be 20 °C, which is the average temperature in the LHC tunnel at IPs 1 and 5. A homogeneously distributed heat flow was applied to the internal surfaces of the absorber's bakeout jackets which corresponds to the heating power computed in Sec. III A [Fig. 8(a)]. Moreover, an adapted heat flow was included on the recombination chamber's bakeout jackets and the end chamber's flange to monitor follow the temperature profile of the bakeout cycle. Convection losses with coefficients of 5 and 3 $\mathrm{W\,m^{-2}\,K}$ were applied along the faces exposed to the LHC tunnel air flow [23] and on the absorber slots, respectively. Radiation between the absorber and BRAN and between the absorber and the lid were included with a 0.72 emissivity (which corresponds to heavily oxidized copper [24]). Finally, a perfect thermal insulation on the vacuum pipes was considered.

The results of the simulations are shown in Figs. 9(b) and 10. The minimum absorber temperature reached in the chamber is 265 °C after a 7 h of bakeout following the temperature profile shown in Fig. 8(a). The proposed system ensures a heating rate of $50\,^{\circ}\mathrm{C\,h^{-1}}$ when required. The temperature reached at the end of the double pipes is lower by a ΔT of less than 25 °C. This effect can be compensated for by reducing the $50\,^{\circ}\mathrm{C\,h^{-1}}$ heating rate to slowly thermalize the copper block and chamber via conduction.

IV. COOLING SYSTEM

Every beam collision performed at the interaction points will deposit a heat load into the TAXN absorber. The deposited heat load must be removed by a water-cooling circuit. The proposed cooling system consists of eight

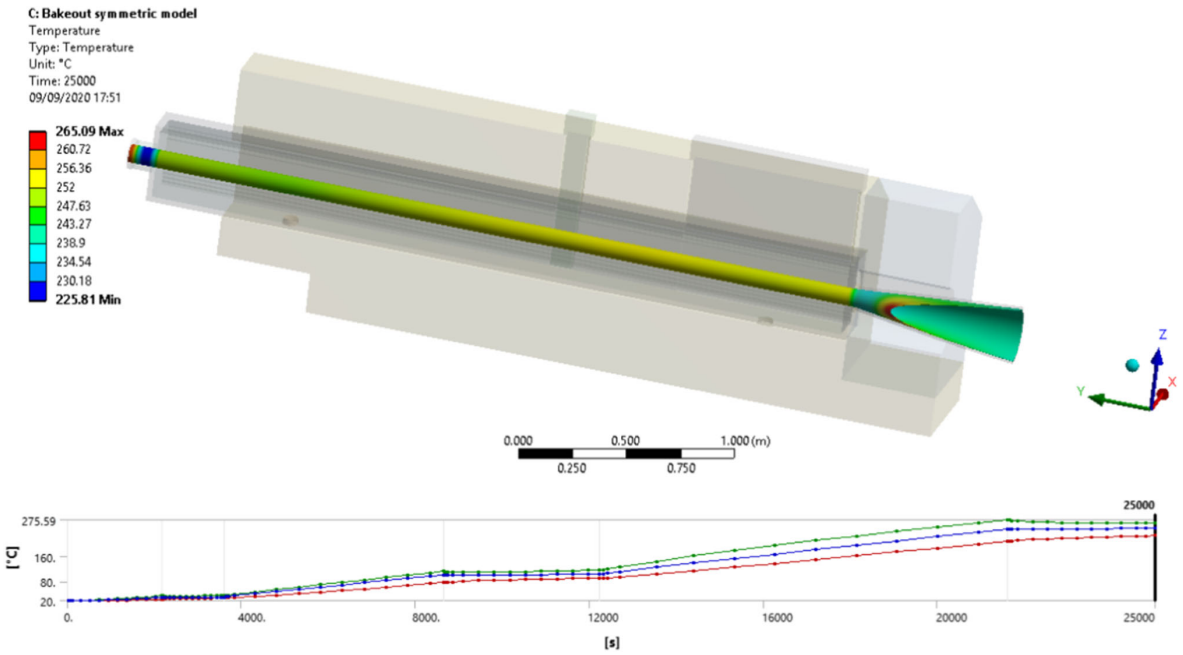

FIG. 10. Temperature distribution along the grooves of the absorber where the vacuum pipe will be clamped during the bakeout cycle.

cooling pipes [Fig. 11(a)], which are connected to the LHC tunnel's demineralized water network. The water flow must be constant during the accelerator's operation. However, the circuit must be emptied during the bakeout cycle to avoid overpressurizing the pipes. The tubes, filled with circulating water, run along the absorber's whole 3.3 m length. According to the results below, the maximum temperature at the vacuum chamber will not be compromised while the cooling system is running. However, constant contact between the absorber and the cooling pipes has to be ensured for an efficient heat transfer, for instance, by applying pressure through a rigid stainless-steel plate [Fig. 11(b)]. Another option can be a spring or clamp system used to adjust and control the applied pressure.

A. Boundary conditions' calculation

The relation between the cooling pipes' diameter (D) and the water velocity (u_m) yields the pipe's water throughput [Eq. (5)]. Consequently, multiplying the throughput by the number of cooling pipes (n) yields the total water flow taken from the LHC tunnel's cooling network [Eq. (6)]. The recommended maximum water flow speed inside a copper pipe is 3 $\mathrm{m\,s^{-1}}$ [25] to avoid high erosion rates of the

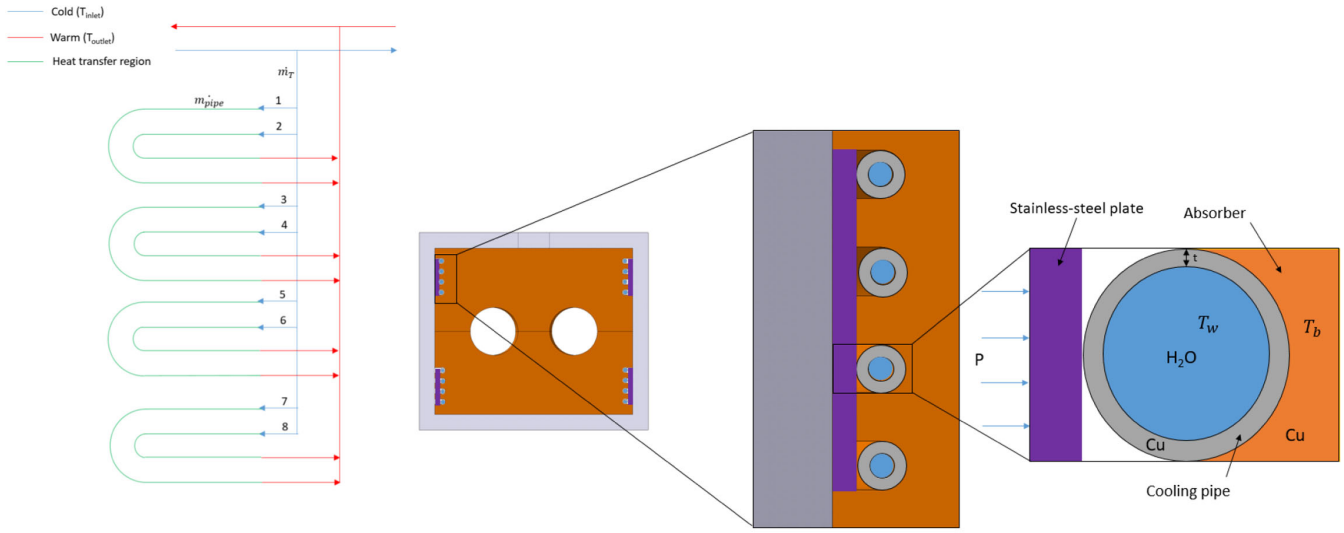

FIG. 11. Proposed cooling system. (a) Demineralized water network (b) Internal scheme of the cooling system.

internal face of the copper pipes. Therefore, 1 m s^{-1} is proposed for maintaining a safety margin. A standard copper pipe of 8 mm of diameter and 1 mm thickness [26] and a total number of eight cooling pipes are considered. The LHC tunnel's cooling line is expected to provide water ($T_{w.\mathrm{inlet}}$) = 27 °C. On the other hand, the expected heat load deposited by the collision debris (Q_{debris}) is about 1800 W (see Sec. II A). Considering a double safety factor for the heat to be removed, using Eq. (7), the expected maximum water temperature increment is $\Delta T = 2.2$ °C, and the water outlet temperature is $T_{w.\mathrm{outlet}} = 29.2$ °C. No heat deposition is expected on the recombination chamber's surface due to its 2 mm thickness.

$$\dot{m_{\mathrm{pipe}}} = \frac{u_{m(\max)} \pi D^2}{4}, \tag{5}$$

$$\dot{m_T} = \dot{m_{\mathrm{pipe}}} n, \tag{6}$$

$$\Delta T = T_{w.\mathrm{inlet}} - T_{w.\mathrm{outlet}} = \frac{Q_{\mathrm{debris}}}{\dot{m_T} c_{p.w}}. \tag{7}$$

Water's boiling point is 177 °C at 9.319 bar [27]. Thus, as the maximum design temperature of the TAXN absorber is 85° C (owing to vacuum requirements) and assuming that the LHC water line is kept at 16 bar, a 10 bar pressured cooling water is sufficient.

The cooling capacity of the system is defined by the heat transfer area, the total heat transfer coefficient between the absorber and the circulating water (HTC_T), and the maximum ΔT between the inlet and outlet cooling water. As the ΔT of the circulating water is below 5° C [computed by Eq. (7)], it is assumed that the water temperature is the average between the inlet and outlet water temperature while the cooling pipe's conduction is neglected.

Equation (8) is used to compute the total heat transfer coefficient, where the thermal contact coefficient between the cooling pipes and the absorber block (TCC) is calculated by the Mikic-Yovanovich correlation [28] for metals. In addition, as turbulent water flow is expected along the cooling pipes, the heat transfer coefficient (HTC) is computed using the Dittus-Boelter correlation [29]. For an average water speed of 1 m s^{-1} and a cooling pipe internal diameter of 8 mm, the Reynolds and Prandtl numbers are 11462 and 4.624, respectively. Therefore, the water convection heat coefficient is 5899 W m^{-2} K along the pipes. As both the absorber and the cooling pipes are made of copper, assuming a contact pressure of 1 MPa between them, the block-cooling pipes' thermal contact coefficient is 7209 W m^{-2} K. The total heat transfer coefficient obtained by Eq. (8) is 3241 W m^{-2} K. Finally, a total heat transfer thermal coefficient of 3200 W m^{-2} K is considered for the simulations (see Sec. IV B).

$$HTC_T = \frac{1}{\frac{1}{HTC} + \frac{1}{TCC}}. \tag{8}$$

B. Computational cooling simulations

A thermal load will be deposited into the TAXN assembly by every particle collision, i.e., every 25 ns on average. If a localized 1.8 kW thermal load heats up the 3 t copper block during a 1 s period, its temperature rises locally by approximately 2.5 °C. Thus, a single beam pulse's impact during the ΔT during 25 ns is negligible. Moreover, the simulation of a single HL LHC run of 2748 bunches requires considerable computational resources and time. Therefore, the ANSYS simulation was run in steady state.

The beam-induced deposited energy density has been obtained from FLUKA simulations and then included as heat generation in W cm^{-3} into the ANSYS model. The peak deposition location was centered and located about 160 mm behind the HL ZDC slot. The initial temperature of the model was assumed to be 27° C, which is the expected LHC cold water-cooling line's temperature. The outlet cooling water's temperature was assumed to be 28.4° C, as computed by Eq. (7). The water cooling was represented by a 3200 W m^{-2} K heat transfer coefficient [as estimated via Eq. (8)] along each of the contact pipe-absorber surfaces. To simulate the worst-case scenario, neither the conduction

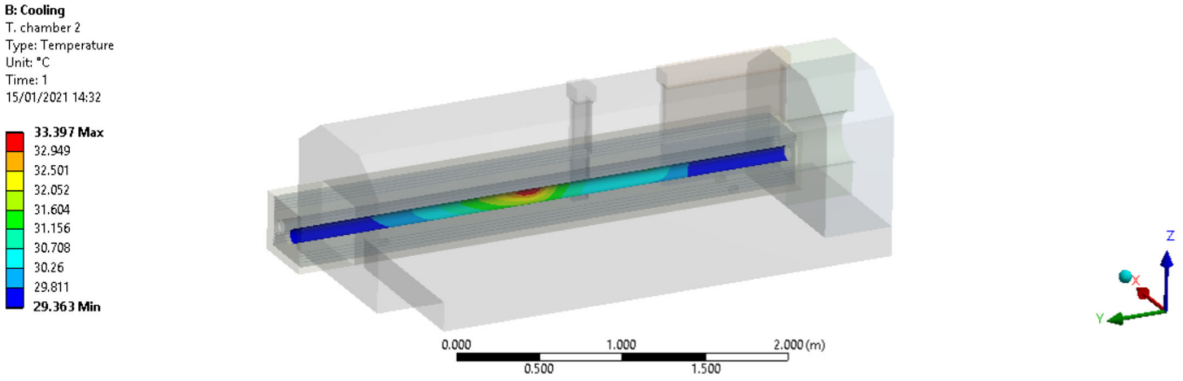

FIG. 12. Simulated temperature distribution along the absorber during the LHC's operation under nominal conditions.

TABLE IV. Summary of the cooling simulation results.

Total heat transfer coefficient [$W\,m^{-2}\,K$]	Number of active cooling pipes	Max temperature in the absorber [°C]	Max temperature on the vacuum chamber [°C]
3200	8	33.8	33.4
3200	4	35.7	35.1
3200	2	38.6	38.0
1000	8	36.4	36.0
500	4	45.4	45.0

on the external pipe's surface of the cooling tubes with respect to the absorber nor the BRAN or lid slot convection have been included in the model. The overall geometry has been slightly modified to increase the mesh adaptability.

The model's mesh size is described in Table III and has an average mesh quality given by the software of 85%.

The results of the simulations are shown in Fig. 12. The maximum expected temperature on the vacuum chamber's surface is about 35° C during the operation of the complete cooling system. In case of a failure scenario where 85% (seven out of eight) of the cooling pipes stop working (but the remaining pipe operates as expected), the maximum expected temperature on the chamber reaches about 65° C. Several scenarios with a varying number of operating cooling pipes and total heat transfer coefficient have been studied. The results are summarized in Table IV.

V. HL ZDC DETECTOR FOR ATLAS AND CMS

A. HL ZDC role in LHC heavy-ion physics program

The ATLAS and CMS heavy-ion programs in LHC runs 1 and 2 have relied extensively on the presence of ZDCs [30,31] located 140 m in both directions from the interaction point. While the detector is sensitive to forward neutral particles, which are predominantly photons and neutrons, the neutron component is the main one observed when requiring energies at or above the per-nucleon beam energy during heavy-ion operation. In a typical heavy-ion collision, producing hundreds or even thousands of final-state particles in the central LHC detectors, the two nuclei have a substantial geometric overlap, in which the protons and neutrons (nucleons) in one nucleus interact inelastically with the nucleons in the other. Each of these inelastic collisions tends to deplete the initial energy of the participating nucleons, which are transformed into an array of final-state hadrons. The nucleons which do not interact suffer no energy loss and primarily keep moving in the far-forward direction, keeping their initial energy but also forming nuclear fragments from the initial excited nuclear remnants. The neutrons which are not bound up in fragment production, which can be as large as 40–50 in each direction in a single event, are registered in the ZDC, with typical deviations from $\theta = 0$ characteristic of their nuclear Fermi energy, which can be up to several hundred MeV in a large nucleus. Since the overlapping area is reflected identically in the two opposing nuclei, the number of neutrons emitted in each direction is very strongly correlated. The number of neutrons in the two arms is also strongly correlated with the number of produced hadrons, many emitted at 90° relative to the beam line.

Hadronic processes provide the typical conditions for producing the quark gluon plasma (QGP), an ultrahot and dense state of matter in which the main degrees of freedom are the quark and gluon constituents of the nucleon rather than the nucleons themselves or other hadrons. A key quantity for characterizing the initial state of the QGP is the size and shape of the collision region at the exact moment of interaction. The quantity that provides information about both of these is the "centrality" of the collision; the most central collisions have the highest multiplicity events, given by the particles measured in the central region. Conversely, events with the lowest multiplicities are the least central or "peripheral." In these events, the number of observed neutrons is similar in the two directions.

There is another distinct class of events at even larger impact parameters, where the nuclei "miss" each other completely and the interactions proceed primarily through interactions of the strong EM fields surrounding one nucleus with either the opposing strong EM field (photon-photon collisions) or the opposing nucleus itself (a photonuclear interaction). In photon-photon events, the leading-order process can produce particles—primarily exclusive states involving leptons, hadrons, or even photons—but generate no activity in either ZDC. In photonuclear processes, the nucleus that emits the photon also remains undisturbed, while the hadronic process tends to break up the other one, leaving final-state neutrons in just one direction. It should be noted that secondary electromagnetic interactions involving soft photons are able to induce nuclear breakup in both cases, even when the breakup is disallowed by the leading-order processes.

Thus, the primary role of the ZDC has been to estimate the number of neutrons per LHC collision event. Using the energy visible in each ZDC, one can define three primary topologies: (i) 0n0n is the case of having no neutrons in either ZDC, indicative of photon-photon processes, (ii) Xn0n/0nXn, when there is a neutron signal in only one side, indicating photonuclear processes, and (iii) XnXn, where both sides show activity. Additional thresholds, e.g., distinguishing events with 1–4 neutrons,

which are typically from soft photoneutron processes from highly inelastic events with five or more neutrons, can also be used.

The primary goals of the ZDC are the identification of the primary physical process (EM, photonuclear, or fully hadronic) and the quantitative estimation of the centrality of hadronic processes. These require only a sufficient containment in the longitudinal and transverse directions to perform a good energy measurement. However, additional capabilities can be provided to the ZDC if additional further segmentation in the front sections of the calorimeter is achieved. Since the radiation length of a photon is much shorter than the interaction length, photons deposit their energies in the front of the first ZDC module and with a limited transverse extent. Thus, introducing longitudinal segmentation and even some limited transverse segmentation can provide discrimination of photons from single neutrons.

Peripheral events are characterized by larger impact parameters, and the overlap region becomes highly anisotropic due to its lenticular (almond) shape. Detailed measurements of the angular distributions of the produced hadrons show that particle production is substantially enhanced in the direction along the impact parameter connecting the nuclear barycenters, as a result of strong pressure gradients along the short axis of the overlap region, which defines the "reaction plane." Estimating this direction is usually performed by looking for a correlated back-to-back enhancement of forward particle emission in the azimuth. However, these particles are correlated only with the reaction plane and, thus, define an "event plane" derived from the final-state particles themselves. To connect back directly to the initial-state geometry, one measures the correlated forward-backward azimuthal deflections of the spectator neutrons. These deflections are small, typically only several millimeters event to event, but they have been found to be observable by the means of a transversely segmented reaction plane detector (RPD), placed at the position where the hadronic showers are typically at their maximum.

B. HL ZDC design

A three-dimensional view of the current design of the HL ZDC is presented in Fig. 13. Contrary to the current ZDCs, the HL ZDC is characterized by a single-unit structure conceived to streamline the craning operations. The detector was designed with a patch panel to allow an ALARA approach during the cabling operations after the craning. All signal, high-voltage, and calibration lines are routed internally to multicore connectors on the patch panel, such that cabling the detector will involve the connection of only a few cables.

The HL ZDC is divided into an electromagnetic (EM) and a hadronic (HAD) section, both relying on tungsten fused silica sampling detection technology. In both units, 1.5-mm-diameter fused silica rods are used as Cherenkov radiators between absorber plates with a thickness of 4 (EM) and 10 mm (HAD). The total depth of tungsten along the beam axis in the EM corresponds to 28.5 radiation lengths and one nuclear interaction length (λ_{int}), while the HAD section includes about 4.5 interaction lengths. The Cherenkov light generated by the charged fraction of the shower in the fused silica rods is internally reflected toward the extremity of the rods. At the top, light guides convey the

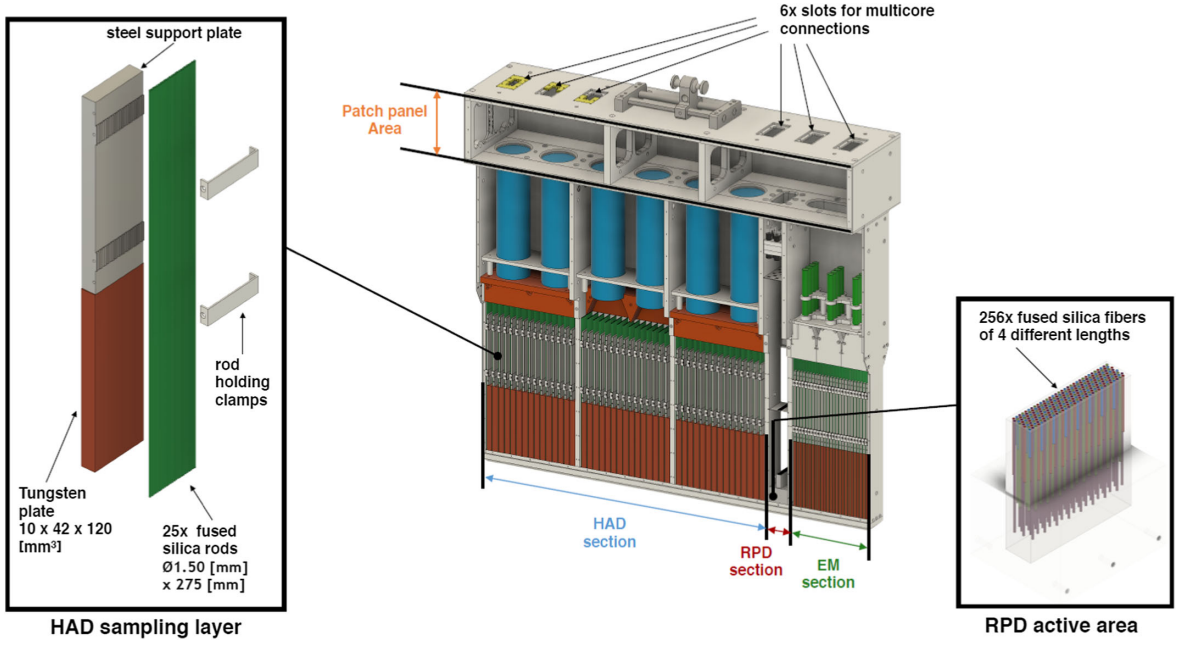

FIG. 13. HL ZDC detector design and details.

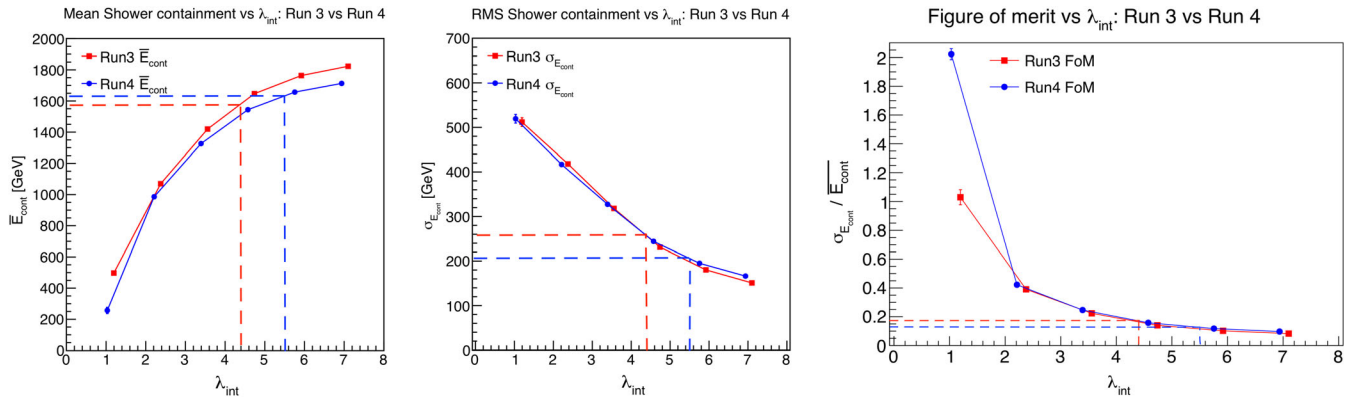

FIG. 14. HL ZDC performance evaluated via Geant4 MC. Comparison of run 3 and run 4 mean (left panel) and standard deviation (central panel) of the energy containment distribution for the ZDC for 2.5 TeV neutrons. Both the current detector and the HL ZDC were simulated with different interaction lengths to determine the detector's performance as a function of the geometry. The ratio between the standard deviation and the mean of the energy containment is used to build the figure of merit of the detector (right panel). See Ref. [34] for more details.

light on the window of photomultiplier tubes (PMTs). The EM section is equipped with Winston cone [32] shaped light guides, laid out on a fourfold horizontal segmentation and three longitudinal subsections to guarantee a high discrimination power between neutrons and photons. The HAD section presents only longitudinal segmentation, implemented by a series of six large area PMTs that detect the light conveyed on their windows by trapezoidal light guides.

In between the EM and HAD sections, the HL ZDC design includes a reaction plane detector. The RPD is installed immediately downstream of the EM module. Its current design consists of an approximately 4×4 cm^2 active region at its base (shown in the right inset in Fig. 13), where the shower of charged particle produced by forward particles interacting in the EM module generates Cherenkov radiation into a staggered array of fused silica fibers. The fibers are not limited to the active area but extend from the active region to the PMTs. Thus, any signal generated in the fibers outside of the bottom 16 cm^2 cannot be used for the x-y mapping of the shower. However, very little hadronic activity is produced in that region, and the spectator neutrons are typically well contained inside the nominal detector volume. The active area of the RPD comprises 256 overlapping fibers that, thanks to the subtraction of the signals on the same vertical coordinate, can be treated as a virtual 4×4 array of square tiles. Therefore, the structure of the signals from the RPD can be interpreted as pixels of an image. Hence, dedicated algorithms using machine-learning techniques such as pattern recognition and computer vision [33] are being developed to reconstruct the reaction plane of heavy-ion collisions from the RPD data.

C. HL ZDC expected performance

The HL ZDC was designed according to different geometrical constraints imposed by the TAXN design (see Sec. II B) compared to the existing TAN. The width of the slot available for the detector will be 46 mm, half of the 92 mm currently available in the TAN. The reduced transverse size impacts the detector performance, worsening the shower containment. Thanks to the large forward Lorentz boost of the spectator neutrons, the shower mainly develops along the longitudinal direction, containing the transverse losses due to the reduced transverse size. Conversely, the TAXN layout enables a single-module detector along the beam pipe without introducing the BRAN between the EM and the HAD section and, therefore, implementing a continuous sampling of the shower along the HL ZDC. Last, the longitudinal size of the available slot can accommodate up to $5.5\lambda_{\mathrm{int}}$ of tungsten, which helps to reduce the detection efficiency and resolution deterioration due to punch through (the current ATLAS and CMS ZDCs are ~4.5 interaction lengths). Dedicated GEANT4 Monte Carlo (MC) studies were carried out to estimate the expected performance of the HL ZDC and compare it with that of the existing detectors. The results are shown in Fig. 14 and can be interpreted in light of the factors described above. The HL ZDC is expected to achieve a better single-neutron resolution compared to the current detectors.

VI. BRAN LUMINOSITY DETECTOR

The BRANs are instruments that measure the relative rate of neutral particles produced by collisions at the four LHC experiments and, therefore, their relative luminosity. BRANs are used by the LHC operations team to find and optimize the collision rate for physics production. Because of the markedly different magnitude of collision rates between the LHC experiments, several different types of BRANs are installed in the machine. This section concerns the ones used for ATLAS and CMS (referred to as "BRAN-Q"), facing the challenge of properly functioning while

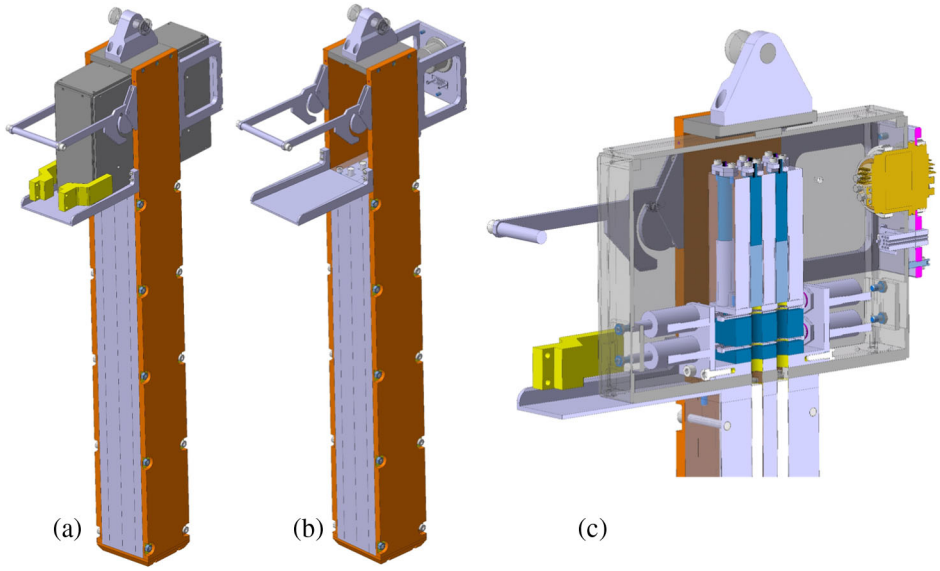

FIG. 15. BRAN-Q prototype assembly (a), featuring the copper enclosure for fused silica rods and the detection box. Assembly with the detection box removed (b), exposing the tip of fused silica rods. Section of the detection box (c).

withstanding the very high dose expected to be reached in the HL LHC scenario.

The principle of the BRAN-Q is to detect the showers produced by the interactions between the neutrals and the TAXN through the Cherenkov radiation emitted by the included fused silica rods. The BRAN-Q's design will be based on a prototype that has been produced for the third LHC run (Fig. 15), even though the latter has dimensions and specific features that are compatible with only the present LHC absorbers. The BRAN prototype is composed of two subsets: a copper enclosure that hosts eight fused silica bars and a removable box that is installed on top of the enclosure and contains the PMTs that detect the Cherenkov radiation produced in the rods. The enclosure [Fig. 15(b)] is inserted in the 100-mm-wide slot of the LHC absorber (TAN) and is equipped with a hook for crane installation or deinstallation. The rods are 10-mm-diameter, 603-mm-long high-purity fused silica with low OH content and no O_2, produced by Haereus, that were selected after a study of the impact of radiation on the optical transmissivity of fused silica [35]. Each BRAN hosts eight rods to provide a transverse spatial resolution and redundancy in the case of single-channel malfunction. Cherenkov radiation produced in each of the fused silica rods is detected by a dedicated PMT hosted in the detection box [Fig. 15(c)]. To cope with the decreased light signal caused by radiation, a variable-aperture iris driven by push solenoids is placed in front of each PMT, allowing one to set the aperture to 100%, 10%, or 1%.

One of the key features of the BRAN prototype is the possibility to install and remove the detection box by the means of the CERNbot [36]. This is a requirement for the HL LHC case due to the higher luminosity. For this purpose, a series of design features are present, such as the use of integrated, nonlatching connectors, a handle to facilitate the installation and removal of the box, and a limitation of the detection box's weight to comply with the CERNbot's limits (a 7 kg payload limit and an 80 N maximum gripping force).

Two BRAN prototypes were installed in the LHC during the 2021–2022 year end technical stop (YETS). They will be followed by two additional ones to be installed in the 2022–2023 YETS. The design of the BRAN-Q will start in 2022, adapting the prototype to the TAXN envelope and specific features (like the wire positioning system and 50-mm-wide slot). Additional possible design modifications or new features will come from the experience gathered with the prototypes during the third LHC run and, to optimize robot handling, through dedicated tests.

VII. CONCLUSIONS

The mechanical design, bakeout, and cooling systems of the TAXN and recombination chamber have been defined in compliance with the vacuum, alignment, heat deposition, radiation protection, and beam aperture requirements under the HL LHC operation conditions. The proposed bakeout system, based on the standard LHC bakeout jackets, allows one to reach a minimum of 250 °C temperature on the recombination chamber's internal surface at a 50 °C h^{-1} heating rate. The bakeout power inputs have been computed analytically and cross-checked by a transient thermal analysis. Nevertheless, temperature tests are to be performed during the prototype phase to validate the thermal behavior of the jackets and absorber together with the

recombination chamber-absorber coupling. In addition, stress tests are recommended to validate the sphere-based supporting system concept of the absorber. Finally, the FEM simulations of the demineralized water-cooling system show that working operational conditions can be maintained in the recombination chamber below 50 °C for a maximum localized heat load of 1.4 kW deposited into the absorber. The loss of coolant analysis concludes that, even if 85% of the cooling pipes completely fail, the maximum expected temperature on the chamber is about 65 °C. The integration in the design of the zero degree calorimeter (HL ZDC) and BRAN luminosity detector have been completed, enlarging the utility of the TAXN as it is located in a very interesting location from the particle physics point of view.

The authors thank Giuseppe Bregliozzi for his valuable comments regarding the future operation of the recombination chamber within the Large Hadron Collider; Frederic Luiz for his contribution to the 3D modeling of the recombination chamber and bakeout jackets; and Thibaut Coiffet from the CERN main workshop for his advice on fabrication-related matters and mechanical tolerance definitions. Finally, many thanks also to Markus Brugger for his support in preparing this article.

[1] G. Apollinari, I. Béjar Alonso, O. Brüning, P. Fessia, M. Lamont, L. Rossi, and L. Tavian, High-Luminosity Large Hadron Collider (HL-LHC) Technical Design Report V.01, 2017, Vol. **4**, p. 599.

[2] O. Brüning, P. Collier, P. Lebrun, S. Myers, R. Ostojic, J. Poole, and P. Proudlock, LHC design report, 2004, Vol. **4**, p. 548.

[3] J. Hansen and P. Santos Diaz, IP1 and 5 recombination chamber conceptual design, CERN internal EDMS document No. 1824656, v.3.1, 2020.

[4] M. Sabate Gilarte and F. Cerutti, Impact on energy deposition in IR1/5 from the new TAXN aperture of 88 mm, ColUSM No. 133, 2020.

[5] G. Battistoni, T. Boehlen, F. Cerutti, P. W. Chin, L. S. Esposito, A. Fassò, A. Ferrari, A. Lechner, A. Empl, A. Mairani, A. Mereghetti, P. Garcia Ortega, J. Ranft, S. Roesler, P. R. Sala, V. Vlachoudis, and G. Smirnov, Overview of the FLUKA code, Ann. Nucl. Energy **82** (2015), available at https://fluka.cern.

[6] T. T. Bohlen, F. Cerutti, M. P. W. Chin, A. Fassò, A. Ferrari, P. G. Ortega, A. Mairani, P. R. Sala, G. Smirnov, and V. Vlachoudis, The FLUKA code: Developments and challenges for high energy and medical applications, Nucl. Data Sheets **120**, 211 (2014).

[7] A. Carvalhosa and A. Amorim Carvalho, QFL magnet support test, CERN internal EDMS document No. 2242728 v.1, 2019.

[8] A. Infantino, HL-LHC TAXN: Shielding requirements verification, CERN internal EDMS document No. 2212244 v.1, 2019.

[9] P. Santos Diaz, M. de la Aleja Cabana, and M. Mendes, TAXN interfaces to BRAN and ZDC, CERN internal EDMS document No. 2349145 v.1, 2020.

[10] General tolerances, part 2: Geometrical tolerances for features without individual tolerance indications, BS EN 22768-2:1993 ISO 2768-2:1989.

[11] Geometrical product specifications (GPS)—Cylindricity—Part 1: Vocabulary and parameters of cylindrical form, ISO 12180-1:2011.

[12] P. Santos Diaz, HL-LHC circular vacuum chamber definition, CERN internal EDMS document No. 1824657 v.1.2, 2017.

[13] B. Spataro, D. Brandt, F. Caspers, D. Li, M. Migliorati, A. Mostacci, L. Palumbo, F. Ruggiero, and L. Vos, On trapped modes in the LHC recombination chambers: Numerical and experimental results, Nucl. Instrum. Methods Phys. Res., Sect. A **517**, 19 (2004).

[14] D. Amorim, S. Antipov, N. Biancacci, B. Salvant *et al.*, HL-LHC impedance and related effects, Report No. CERN-ACC-NOTE-2018-0087, 2018.

[15] B. Salvant, Beam impedance simulation for the HL-LHC recombination chamber, CERN internal EDMS document No. 2315010 v.1, 2020.

[16] A. Rossi, Residual gas density estimations in the LHC insertion regions IR1 and IR5 and the experimental regions of ATLAS and CMS for different beam operations, CERN LHC Project Report No. 783, 2004.

[17] A. Rossi, Residual gas density estimations of the LHC experimental interaction regions, CERN LHC Project Report No. 674, 2003.

[18] G. Bregliozzi, Bake-out and NEG vacuum activation of the LSS vacuum sectors, CERN internal EDMS document No. 1251378 v.7, 2019.

[19] Python Software Foundation, Python Language Reference, version 3, available at http://www.python.org.

[20] N. Zelko, DO-26476/TE technical specification for the supply of heating jackets for the LHC test bench extension, CERN internal EDMS document No. 1133805 v.1, 2011.

[21] N. Zelko, Technical specification for the coaxial thermocouple type E "standard", CERN internal EDMS document No. 1509433 v.1, 2015.

[22] ANSYS Inc., Ansys Academic Research Mechanical and CFD, release 2019 R1, available at https://www.ansys.com.

[23] M. Nonis, Modification of the LHC underground ventilation system, Chamonix 2010 workshop on LHC performance, Report No. CERN-ATS-2010-026, Chamonix, 2010.

[24] Table of emmisivity of various surfaces, Transmetra, https://www.transmetra.ch/images/transmetra_pdf/publikationen_literatur/pyrometrie-thermografie/emissivity_table.pdf.

[25] L. Knutsson, E. Mattsson, and B-E. Ramberg, Erosion corrosion in copper water tubing, British Corrosion Journal **7**, 208 (1972).

[26] KME, TECTUBE industrial tubes made from copper and copper alloys, https://www.kme.com/fileadmin/DOWNLOADCENTER/COPPER%20DIVISON/5%20Industrial%20Tubes/1%20TECTUBE%C2%AE/TECTUBE_Industrierohre/TECTUBE_Industrial_Tubes_2016_EN.pdf.

[27] Sixth edition, Fundamentals of Heat and Mass. Transfer. Frank P. Incropera, College of Engineering, University of Notre Dame, David P. Dewitt, Table A.6.
[28] M. G. Cooper, B. B. Mikic, and M. M. Yovanovich, Thermal contact conductance, Int. J. Heat Mass Transfer **12**, 279 (1969).
[29] W. H. McAdams, *Heat Transmission*, 3rd ed. (McGraw-Hill, New York, 1954).
[30] ATLAS Collaboration, The ATLAS Experiment at the CERN Large Hadron Collider, J. Instrum. **3**, 214 (2008).
[31] O. Surányi *et al.*, J. Instrum. **16** (2021) P05008.
[32] W. T. Welford and R. Winston, *The Optics of Nonimaging Concentrators: Light and Solar Energy* (Academic, New York, 1978), OSTI ID: 5380269.
[33] Christopher M. Bishop, *Pattern Recognition and Machine Learning* (Springer, New York, 2006).
[34] ATLAS Collaboration, A radiation-hard zero degree calorimeter for ATLAS in the HL-LHC era, Report Nos. CERN-LHCC-2021-018, LHCC-P-019, 2021.
[35] S. Yang *et al.* (to be published).
[36] V. Baldassarre, Cernbot functional specifications, CERN internal EDMS document No. 2443863 v.1, 2021.